Bone tumor-homing nanotherapeutics for prolonged retention in tumor microenvironment and facilitated apoptotic process *via* mevalonate pathway inhibition

Nae-Won Kang [a], Voradanu Visetvichaporn [a], Duy-Thuc Nguyen [a], Eun Kyung Shin [a], Da-Han Kim [a], Min-Jae Kim [a], So-Yeol Yoo [b], Jae-Young Lee [b,*], Dae-Duk Kim [a,**]

[a] *College of Pharmacy and Research Institute of Pharmaceutical Sciences, Seoul National University, Seoul, 08826, Republic of Korea*
[b] *College of Pharmacy, Chungnam National University, Daejeon 34134, Republic of Korea*

ABSTRACT

Bone malignancy features a mineralized extracellular matrix primarily composed of hydroxyapatite, which interferes with the distribution and activity of antineoplastic agents. Herein, we report bone tumor-homing polymeric nanotherapeutics consisting of alendronate-decorated chondroitin sulfate A-graft-poly(lactide-co-glycolide) and doxorubicin (DOX), named PLCSA-AD, which displayed a prolonged retention profile in the tumor microenvironment and augmented therapeutic efficacy *via* inhibition of the mevalonate pathway. PLCSA-AD exhibited a 1.72-fold lower IC_{50} value than free DOX and a higher affinity for hydroxyapatite than PLCSA in HOS/MNNG cell-based 2D bone tumor-mimicking models. The inhibition of the mevalonate pathway by PLCSA-AD in tumor cells was verified by investigating the cytosolic fraction of unprenylated proteins, where blank PLCSA-AD significantly increased the expression of cytosolic Ras and RhoA without changing their total cellular amounts. In a bone tumor-mimicking xenografted mouse model, AD-decorated nanotherapeutics significantly increased tumor accumulation (1.73-fold) compared with PLCSA, and higher adsorption to hydroxyapatites was observed in the histological analysis of the tumor. As a result, inhibition of the mevalonate pathway and improvement in tumor accumulation led to markedly enhanced therapeutic efficacy *in vivo*, suggesting that PLCSA-AD could be promising nanotherapeutics for bone tumor treatment.

1. Introduction

The highly mineralized extracellular matrix of malignant bone tumors is composed primarily of hydroxyapatites ($Ca_{10}(PO_4)_6(OH)_2$), whose physicochemical properties can modulate tumor progression [1]. For the treatment of malignant bone tumors, various anticancer agents, including doxorubicin, methotrexate, and cisplatin, are recommended as first-line treatment options [2]. However, the mineralized matrix of the bone tumor hinders the accumulation of anticancer agents, resulting in limited therapeutic effect and drug resistance [3]. Therefore, practical strategies for enhancing the drug distribution to bone tumors and antitumor efficacy are required to achieve an effective cancer therapy.

Among the various strategies, mevalonate pathway inhibition is an effective option for bone cancer treatment, resulting in the promotion of tumor apoptosis. The mevalonate pathway plays a central role in cellular

metabolism, providing essential metabolites for multiple cellular processes [4]. Thus, inhibition of the mevalonate pathway in tumor cells would affect cell viability and increase tumor-suppressive effects [5]. The representative mevalonate pathway inhibitors are nitrogen-containing bisphosphonates that interfere with the post-translational prenylation of small GTP-binding proteins [6]. In addition, the bisphosphonate groups of these compounds can form strong ionic interactions with hydroxyapatite, thereby increasing their biodistribution to the mineralized matrix of the bone. However, the agents themselves show low cellular availability because of their hydrophilic and negatively charged features, which impede their access to the cell membrane [7,8]. In this regard, bisphosphonate-containing biomaterials that can promote cellular uptake efficiency and inhibit the mevalonate pathway are required for effective bone tumor therapy.

Chondroitin sulfate A (CSA) is a biocompatible and biodegradable

---

glycosaminoglycan that can bind to CD44 receptors, which are overexpressed on the surface of various tumor cells, including osteosarcoma [9–12]. As the CSA–CD44 interaction triggers endocytosis, this mechanism can be exploited to introduce cargo molecules (*i.e.*, adsorbed or conjugated to CSA) into tumor cells, regardless of their hydrophilicity [9]. Moreover, our previous study confirmed the liberation of both conjugated and adsorbed cargo molecules from polysaccharide derivatives upon endolysosomal uptake, by which they regain their unique activities against cancer cells [13]. Therefore, we hypothesized that nanotherapeutics (NTs) composed of CSA might efficiently deliver conjugated bisphosphonates, as well as loaded antineoplastic agents, into bone tumor cells [14,15].

Previously reported nanoplatforms for bone cancer treatment have tended to focus only on the targeting ability to the bone tumor microenvironment (TME). However, alendronate-decorated polylactide-co-glycolide-conjugated chondroitin sulfate A (PLCSA-AD) that we report here is an advanced bone-TME targeted NT with innate tumor-suppressive activities (Fig. 1). We decorated alendronate (AD) on the surface of the NTs to enhance the bone tumor targetability and efficacy based on the following rationales: (1) Due to its clinical availability and high pharmacological potency, AD was considered to be a preferred option for treating bone-related diseases [16]; (2) The molecular structure of AD features a primary amine end, which confers inhibitory effects on farnesyl diphosphate synthase in the mevalonate pathway and on bone-resorbing osteoclasts [16–18]; and (3) two phosphonate groups within the structure are capable of forming strong charge-charge interactions with hydroxyapatites in the bone TME, leading to improved tumor distribution and retention [19].

Moreover, the CSA shell of PLCSA-AD could interact with CD44 receptors on bone tumor cells, promoting endocytosis. In tumor cells, NTs could be degraded by endolysosomal enzymes, followed by the release of AD and doxorubicin (DOX), a cargo antineoplastic drug. The released AD would inhibit the mevalonate pathway in tumor cells, enhancing the anticancer activity of DOX. Improved targeting ability to the bone TME and enhanced apoptotic processes *via* inhibition of the mevalonate pathway were demonstrated using various *in vitro* and *in vivo* bone tumor-mimicking models.

2. Materials and methods

2.1. Materials

CSA (average 37 kDa), 1-ethyl-3-(3-dimethylaminopropyl) carbodiimide (EDC), *N*-hydroxysuccinimide (NHS), hydroxyapatite, and triethylamine (TEA) were purchased from Sigma-Aldrich (St. Louis, MO, USA). Poly(lactide-co-glycolide)-diamine (PLGA-NH$_2$; 5000 – 10,000 Da) was obtained from Akina (West Lafayette, IN, USA). AD (sodium trihydrate form) was purchased from Tokyo Chemical Industry Co. Ltd. (Tokyo, Japan). DOX (HCl salt) was obtained from LC Laboratories (Woburn, MA, USA).

2.2. Synthesis of PLCSA-AD

PLCSA-AD was synthesized *via* an EDC/NHS coupling reaction. Briefly, CSA (37.5 mg) was dissolved in formamide (FA; 3.6 mL) at 100 °C and cooled to room temperature. PLGA-NH$_2$ (60 mg) was dissolved in dimethyl sulfoxide (DMSO; 1.2 mL). EDC (20.6 mg) and NHS (12.4 mg) were added to the CSA solution and the mixture was stirred for 30 min to activate the carboxylic acids. Subsequently, PLGA-NH$_2$ and TEA (29.91 μL) were added slowly to the mixture and stirred at 45 °C for 24 h. AD was conjugated to the PLCSA, where EDC (10.3 mg) and NHS (6.2 mg) were added to the mixture and the AD solution was added dropwise, followed by incubation for 24 h. For the preparation of PLCSA, this step proceeded without the addition of AD. After the reaction, the mixture
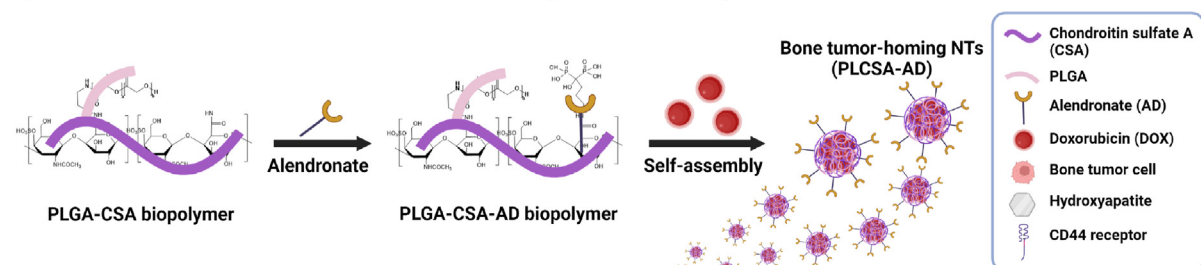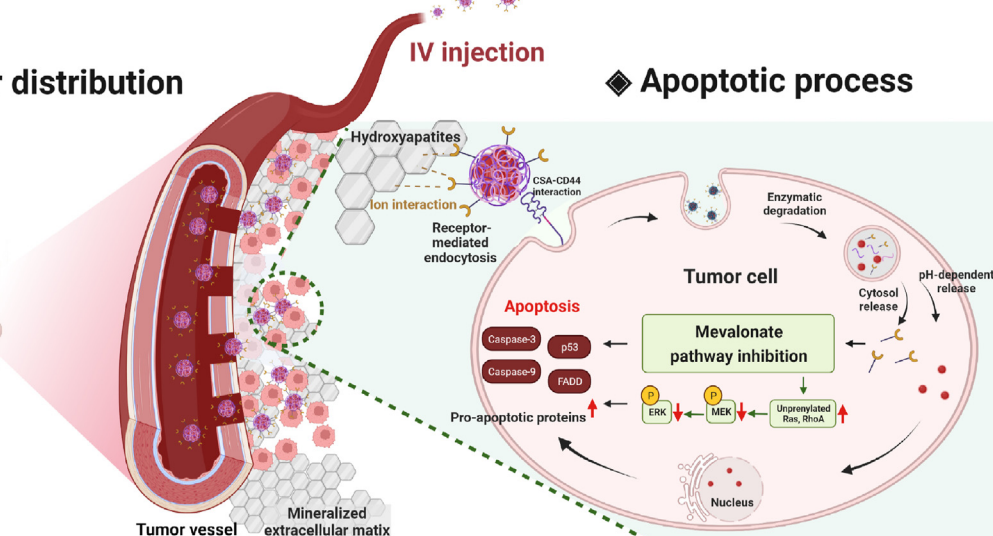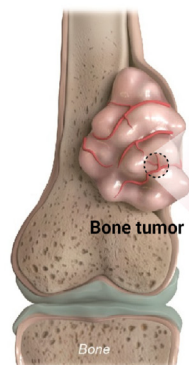

Fig. 1. Schematic illustration of the strategies of bone tumor-homing nanotherapeutics.

was dialyzed (molecular weight cut-off: 12–14 kDa) against water for 48 h and lyophilized. The lyophilized powder was washed twice with acetone to remove unreacted PLGA-NH$_2$ and lyophilized again to obtain PLCSA or PLCSA-AD powder. The resulting white powder was stored at 4–8 °C until further use. The synthesized polymer was evaluated using proton nuclear magnetic resonance (^{1}H NMR; Varian FT-500 MHz; Varian, Inc., Palo Alto, CA, USA) and phosphorus-31 nuclear magnetic resonance (^{31}P NMR; Avance III-500; Bruker, Billerica, MA, USA).

2.3. Preparation and characterization of DOX-loaded PLCSA and PLCSA-AD

DOX base was used as a model hydrophobic anticancer agent. DOX base was prepared from DOX HCl and separated using a liquid-liquid extraction method. Briefly, DOX HCl (60 mg) was dissolved in DW (10 mL) and TEA (50 μL) was added. Then, chloroform (40 mL) was added, and the mixture was vigorously mixed. The chloroform phase was collected and evaporated completely using a rotary evaporator. The red precipitate was dissolved in dimethyl sulfoxide (DMSO) and lyophilized.

To prepare DOX-loaded PLCSA and PLCSA-AD, DOX (1 mg) and polymer (5 mg) were dissolved in a mixture of DMSO and FA (1 mL, 1:1, v/v). The solvent was evaporated under a N$_2$ gas stream for 24 h at 70 °C to obtain a drug/polymer composite film. The film was resuspended in DW (1 mL) by conducting tip sonication (SONICS & MATERIALS, Inc., Newtown, CT, USA), and the resulting suspension was filtered through a syringe filter (0.45-μm pore size; Minisart RC 15, Sartorius Stedim Biotech GmbH, Goettingen, Germany).

To measure the entrapment efficiency, the dispersion of NTs was disrupted with DMSO (50 times volume), and the concentration of DOX was analyzed using a high-performance liquid chromatography (HPLC) system equipped with a separation module (Waters e2695; Waters Co., Milford, MA, USA), fluorescence detector (Waters 2475; Waters Co.), and reverse-phase C18 column (Xbridge RP18, 250 × 4.6 mm, 5 μm; Waters Co.). The mobile phase comprised 1 mM potassium phosphate buffer (pH 2.5, adjusted with phosphoric acid) and acetonitrile with 0.1% TEA (71:29, v/v). The flow rate was set to 1.0 mL/min, and the injection volume was 20 μL. The eluent was monitored at excitation and emission wavelengths of 470 nm and 565 nm, respectively. Particle size and zeta potential were measured using an ELS-Z (Otsuka Electronics, Osaka, Japan).

The morphology of the NTs was observed by field-emission transmission electron microscopy with energy-dispersive spectroscopy (FE-TEM; JEOL, Tokyo, Japan). The samples were prepared on a copper grid with a carbon film, and atomic analyses were conducted on oxygen and phosphorus. The colloidal stability of the developed NTs was tested in phosphate-buffered saline (PBS) and 20% fetal bovine serum (FBS; ATCC, Manassas, VA, USA) in PBS for 24 h to assess the changes in particle size. Mean hydrodynamic diameter and polydispersity index (PDI) were measured using an ELS-Z instrument (Otsuka Electronics).

In vitro DOX release patterns from the NTs were evaluated using mini-GeBAflex tubes (molecular weight cut-off: 14 kDa; Gene Bio-Application Ltd., Yavne, Israel). The NT suspension (100 μL) was loaded into the tube and immersed in PBS at various pH values (30 mL; pH 5.5, 6.8, and 7.4, adjusted with phosphoric acid), followed by incubation in a shaking water bath at 37 °C (50 rpm). Aliquots of the release medium (0.2 mL) were collected at 2, 4, 6, 8, 24, and 48 h, and the same amount of fresh medium was replenished at each time. The amount of DOX in each sample was analyzed using HPLC. The profile of the cumulative drug release (F; %) over time (t) was fitted using mathematical models, the equations of which are as follows:

First − order model : $F = F_{max} \times \left(1 - e^{-kt}\right)$

Higuchi model : $F = k_H \times t^{0.5}$

Baker–Lonsdale model : $\dfrac{3}{2}\left[1 - \left(1 - \dfrac{F}{100}\right)^{\frac{2}{3}}\right] - \dfrac{F}{100} = k_{BL} \times t$

Korsmeyer–Peppas model : $F = k_{KP} \times t^n$

Peppas–Sahlin model : $F = k_1 \times t^m + k_2 \times t^{2m}$

where F_{max} is the maximum cumulative release and k, k_H, k_{BL}, k_{KP}, k_1, and k_2 are the release rate constants of the corresponding models.

2.4. Cellular experiments

HOS/MNNG, a human osteosarcoma cell line, was obtained from ATCC and cultured in Eagle's minimum essential medium (EMEM; ATCC, Manassas, Virginia, USA) supplemented with 10% FBS (ATCC) and 1% PS (Welgene, Gyeongsan-si, Republic of Korea) at 37 °C in a 5% CO$_2$ atmosphere. The distribution of DOX in HOS/MNNG cells and hydroxyapatite was visualized using a confocal laser scanning microscope (CLSM; TCS8; Leica Microsystems, Wetzlar, Germany). We used an *in vitro* bone tumor microenvironment-mimicking cell culture model to simulate the behavior of NTs in the bone TME. Briefly, hydroxyapatite beads (1 mg) and collagen solution (10 μg; Corning Inc., Corning, NY, USA) were mixed and evenly dispersed onto a cell culture slide (2 cm^2). The liquid phase was then completely dried at 25 °C for 24 h to obtain hydroxyapatite-coated slides. HOS/MNNG cells (3 × 10^5 cells) were cultured on hydroxyapatite-coated slides for 24 h and treated with the DOX solution or DOX-loaded NT suspension at a DOX concentration of 20 μg/mL. To verify chondroitin sulfate-mediated cellular uptake, free CSA was used as a competitive inhibitor. After incubation for 1 h, the cells were washed gently with PBS and fixed in a 4% (v/v) formaldehyde solution for 3 min. Cell nuclei were stained with 4,6-diamidino-2-phenyl-indole (DAPI; Vector Laboratories, Burlingame, CA, USA). Z-stack observations were performed at a depth of 20 μm to combine multiple images captured at various focal distances.

For relative quantification of cellular uptake, HOS/MNNG cells (1.5 × 10^5 cells) were cultured in a 6-well plate. The DOX solution or DOX-loaded NTs (20 μg/mL DOX) were incubated at 37 °C for 1 and 3 h. After incubation, the cells were rinsed twice with PBS and trypsinized from the plate, followed by centrifugation at 1000 ×g for 5 min. The cell pellets were resuspended in PBS containing 2% FBS and analyzed using a FACS Calibur flow cytometer (BD Biosciences, San Jose, CA, USA).

To count apoptotic cells after treatment, HOS/MNNG cells (3.0 × 10^5 cells) were cultured in a 6-well plate, followed by treatment with DOX solution or DOX-loaded NTs. The cells were incubated at 37 °C for 72 h. The cells and supernatant were collected and stained with the Annexin V-FITC Early Apoptosis Detection Kit (Cell Signaling Technology) according to the manufacturer's protocol. The prepared samples were analyzed using BD FACS Lyric (BD Biosciences).

The *in vitro* antitumor activity of DOX-loaded NTs was evaluated using the 3-(4,5-dimethyl-2-yl)-5-(3-carboxymethoxyphenyl)-2-(4-sulfophenyl)-2H-tetrazolium (MTS) assay. HOS/MNNG cells were seeded in 96-well plates and incubated for 72 h with DOX solution or DOX-loaded NTs at various DOX concentrations (0.2, 1, 2, 3, and 4 μM). After removing the treated solution, MTS reagent (Cell Titer 96 AQueous One Solution Reagent; Promega, Madison, WI, USA) was added to the cells, and they were incubated at 37 °C for 4 h. The absorbance of each well was measured at 490 nm using a UV–Vis spectrophotometer (EMax Precision Microplate Reader; Molecular Devices). The drug concentration at 50% of maximum inhibition (IC$_{50}$) was calculated using Prism 8.0.2 (GraphPad Software, San Diego, CA, USA).

2.5. Affinity for hydroxyapatite

The affinity of PLCSA-AD for hydroxyapatites was evaluated by analyzing the amount of DOX adsorbed onto hydroxyapatites by flow

cytometry. PLCSA and PLCSA-AD (2.5, 5, 10, and 25 μg/mL DOX) were incubated with hydroxyapatite beads (2 mg) under vigorous vortex mixing for 1 min. The hydroxyapatites were sorted and quantified using FACS Calibur (BD Biosciences) in the fluorescence-2 channel to detect DOX signals.

2.6. Western blot

HOS/MNNG cells (3.0×10^5 cells) were cultured in 6-well plates. For analysis of apoptotic markers, DOX solution or DOX-loaded NTs (4 μM as DOX) were incubated at 37 °C for 72 h. Similarly, for the analysis of intermediates of the mevalonate pathway, the cells were treated with blank biopolymers at four different concentrations of PLCSA or PLCSA-AD (0, 200, 500, and 1000 μg/mL) at 37 °C for 72 h. The cells were washed with PBS and lysed with RIPA lysis buffer containing a protease inhibitor, followed by probe sonication for 10 s under ice. The samples were incubated under ice conditions for 30 min and centrifuged at 13,000 rpm at 4 °C for 10 min. The total protein concentration of the supernatant was measured using a BCA assay kit (Thermo Fisher Scientific, Waltham, MA, USA). Aliquots of the sample solution were collected and subjected to denaturation at 42 °C for 30 min. The prepared samples were loaded (20 μg of total protein) and separated by SDS-PAGE and transferred to polyvinylidene fluoride membranes (Millipore, Burlington, MA, USA). The membrane was incubated with 5% non-fat milk at room temperature for 60 min to prevent non-specific protein binding, followed by incubation with primary rabbit antibodies against p53, Fas-associated death domain (FADD), caspase-9, caspase-3, RhoA, Ras, phosphorylated extracellular signal-regulated kinase 1/2 (phospho-p44/42 MAPK (Erk1/2) (Thr202/Tyr204)), the phosphorylated mitogen-activated protein kinase (phospho-MEK1/2 (Ser217/221)), beta-actin, or glyceraldehyde-3-phosphate dehydrogenase (GAPDH) at 4 °C overnight. The membrane was washed with Tris-buffered saline containing 0.1% Tween 20 and incubated with anti-rabbit IgG and horseradish peroxidase (HRP)-linked antibodies at room temperature for 2 h. After washing with Tris-buffered saline containing 0.1% Tween 20, the membrane was treated with HRP substrate (Thermo Scientific™ SuperSignal™ West Femto Maximum Sensitivity Substrate, Thermo Scientific, Waltham, MA, USA) and analyzed using ImageQuant (LAS4000, GE Healthcare, Chicago, IL, USA). Anti-p53, FADD, caspase-3, caspase-9, beta-actin, GAPDH, Ras, RhoA, *p*-ERK, and *p*-MEK were purchased from Cell Signaling Technology (Danvers, MA, USA).

For the analysis of cytosolic proteins, the cells were rinsed once with PBS and trypsinized from the plate, followed by centrifugation at 1000 $\times g$ for 5 min. The pellet was reconstituted in PBS and centrifuged again ($1000 \times g$ for 5 min). Cytosolic proteins were extracted from the pellet using NE-PER Nuclear and Cytoplasmic Extraction Reagents (Thermo Scientific, Waltham, MA, USA) according to the manufacturer's protocol. The quantification and western blot protocols for the extracted cytosolic protein samples were the same as those described above.

2.7. Animal model

BALB/c nude mice (female, 5 weeks old; Nara Biotech, Seoul, Republic of Korea) were reared in a light-controlled room at a temperature of 22 ± 2 °C and a relative humidity of 55 ± 5% (Animal Center for Pharmaceutical Research, College of Pharmacy, Seoul National University, Seoul, Republic of Korea) to establish heterotopic bone tumor xenograft models. The animal experimental protocol (SNU-210121-10-1) was approved by the Animal Care and Use Committee of Seoul National University. The heterotopic bone tumor model was prepared by subcutaneous inoculation of the tumor cell suspension with bone matrix components in the lower right flank of the mice. The suspension consisted of HOS/MNNG cells (5×10^6 cells) and hydroxyapatite beads (2 mg) dispersed in a mixture of culture medium and Matrigel (1:1, v/v; total volume of 0.1 mL) under cold conditions. Hydroxyapatites were

washed with ethanol and dried overnight to prevent microbial contamination before use.

2.8. Near-infrared fluorescence (NIRF) imaging

The behavior of Cy5.5-labeled NTs was monitored in a heterotopic model. Briefly, Cy5.5-amine (300 μg; Flamma® 675 NHS ester; BioActs, Incheon, Republic of Korea) was conjugated to CSA *via* an EDC/NHS coupling reaction in the final step of the synthesis, and all other steps were the same as described in the Section *Synthesis of PLCSA-AD*. The final product was dialyzed in DW for three days and filtered (0.45 μm) to remove the unreacted Cy5.5-amine completely. The resulting NIRF dye-tagged NTs were administered into the tail vein of tumor-bearing mice at a Cy5.5 dose of 0.1 mg/kg after the tumor volume reached 100–150 mm^3, which was calculated as follows: $0.5 \times$ longest diameter $\times$ (shortest diameter)^2. The whole body was scanned using a VISQUE InVivo Smart (Vieworks, Anyang, Korea) equipped with CleVue™ software (Vieworks) at 0, 1, 3, 6, 9, and 24 h post-injection. The mice were euthanized 24 h after injection, and their tumors and major organs (heart, liver, kidney, lung, and spleen) were dissected for *ex vivo* analysis. For histological analysis, the tumors were sectioned and stained with alizarin red S (Sigma-Aldrich). The distribution of Cy-labeled NTs inside the tumors was observed using CLSM (TCS8; Leica Microsystems).

2.9. In vivo antitumor efficacy

In vivo antitumor efficacy was evaluated using a hydroxyapatite-containing tumor model. The tumor volume (mm^3) and body weight (g) of the mice were monitored daily after inoculation. The experimental groups included PBS (control), DOX solution, PLCSA, and PLCSA-AD. The formulations were administered intravenously at a DOX dose of 5 mg/kg on days 5, 7, and 9. On day 12, the tumor tissues of each mouse were excised and weighed. Tumors and major organs, including the heart, liver, kidney, and spleen, were sliced and stained for histological analysis. The terminal deoxynucleotidyl transferase dUTP nick-end labeling (TUNEL) assay was performed on the tumor tissues, and other organs were stained with hematoxylin and eosin (H&E).

2.10. Antibody microarray analysis

Protein expression patterns in tumors after treatment were investigated using the Signaling Explorer Antibody Array Kit (Fullmoon Biosystem, Inc., Sunnyvale, CA, USA). To prepare the samples, the DOX solution or NTs were intravenously injected (5 mg/kg as DOX) daily for three days into the bone tumor-mimicking mice after the tumor volume reached 100–150 mm^3. PBS-treated mice were used as the control group for the fold-change analyses. One day after the final treatment, each tumor was dissected, and the soluble proteome was collected with protein extraction buffer (Fullmoon Biosystems) containing 1% phosphatase inhibitor cocktail (Sigma-Aldrich), 1% protease inhibitor cocktail (Sigma-Aldrich), and lysis beads (Fullmoon Biosystems). The extracted protein was purified using a gel matrix column. The column matrix was pre-rinsed by vortex mixing for 5 s, hydrated for 60 min at room temperature, and centrifuged at 750 $\times g$ for 2 min. The column was then moved into a collection tube, to which an aliquot (100 μL) of the protein sample was loaded. The column was centrifuged at 750 $\times g$ for 2 min. The protein concentration of the purified samples was determined with a BCA protein assay kit (Pierce, Rockford, IL, USA) using a NanoPhotometer™ (Implen GMBH, Munich, Germany). The purity of the samples was assessed based on the UV absorbance. The prepared samples were subjected to an antibody microarray assay according to the manufacturer's protocol. The intensities of the array slides were analyzed using a GenePix 4100A scanner (Molecular Devices, San Jose, CA, USA) at a resolution of 10 μm. Scanned images were quantified using GenePix software (version 7.0; Molecular Devices) and annotated using the UniProt

database (UniProt Consortium). Data mining and visualization were performed using ExDEGA (Ebiogen Inc., Seoul, Korea). Gene set enrichment analysis (GSEA) was conducted using GSEA 4.1.0 software (Broad Institute, Inc., MA, USA).

2.11. Statistical analysis

All experiments were performed at least three times, and data are presented as the mean $\pm$ standard deviation (SD). Statistical analyses were performed using analysis of variance (ANOVA) with Tukey's multiple comparison test or a two-tailed *t*-test. Statistical significance was set at $p < 0.05$.

3. Results and discussion

3.1. Synthesis and characterization of PLCSA-AD

In this study, PLGA was employed for drug encapsulation and sustained release [20]. AD and PLGA-NH₂ were grafted to the CSA backbone *via* amide bond formation to synthesize the amphiphilic graft copolymer PLCSA-AD (Fig. 2a). The successful conjugation of PLGA was verified by ¹H NMR, where the characteristic peaks of CSA (a, 1.8 ppm of –CH₃; b, 8.2 ppm of –NHCO), PLGA (c, 1.0–1.1 ppm of –CH₂; d, 2.7 ppm of –CH₃), and amide bonds (e, 8.0–8.1 ppm) were identified (Fig. 2b). The composition of CSA and PLGA in the copolymer was calculated to be 1:0.56, by comparing the integration of peaks a and c. The phosphorus peak from the bisphosphonate of PLCSA-AD (f, −0.749 ppm) was detected by ³¹P NMR (Fig. 2c), whereas no peak was observed in PLCSA (*i.e.*, the CSA-PLGA copolymer without AD decoration) (Fig. S1). Moreover, the chemical shift of PLCSA-AD was quite different from that of free AD (18.2 ppm; Fig. S1), implying the successful conjugation of AD to PLCSA.

After DOX loading, the NTs exhibited a spherical morphology with a unimodal size distribution (Fig. 3a and b), suggesting the successful self-assembly of the developed polymers. The observed PLCSA-AD was further investigated by atomic analysis, where white, green, and red colors indicate the bright field, oxygen, and phosphorus, respectively (Fig. 3c). The intensity of phosphorus is likely derived primarily from the AD moieties ($C_4H_{12}NO_7P_2$), whereas the carbon and oxygen signals likely arise from all components, including AD, CSA (monomer: $C_{14}H_{23}NO_{15}S$), PLGA (monomer: $C_5H_8O_5$), and DOX ($C_{27}H_{29}NO_{11}$). The presence of a phosphorus signal in the overlapped image supports the existence of a surface AD. Fig. 3d presents details of the physicochemical properties of the developed NTs. PLCSA-AD showed a mean diameter of 217.9 ± 4.6 nm with a polydispersity index (PDI) value of 0.15 ± 0.02. Although PLCSA exhibited a larger mean diameter of 266.8 ± 2.4 nm with a PDI value of 0.12 ± 0.01, the particle sizes of both NTs were considered suitable for size-dependent distribution through inter-endothelial gaps in the tumor vasculature [21]. Of note, PLCSA-AD exhibited more negatively charged zeta-potential values ($−35.1 \pm 2.3$ mV) than did PLCSA ($−20.0 \pm 1.2$ mV), which could result from the anionic feature of surface AD moieties under physiological conditions. The greater negative surface charge would increase electrostatic repulsive forces and thus contribute to the colloidal stability in biological fluids [22]. The developed NTs
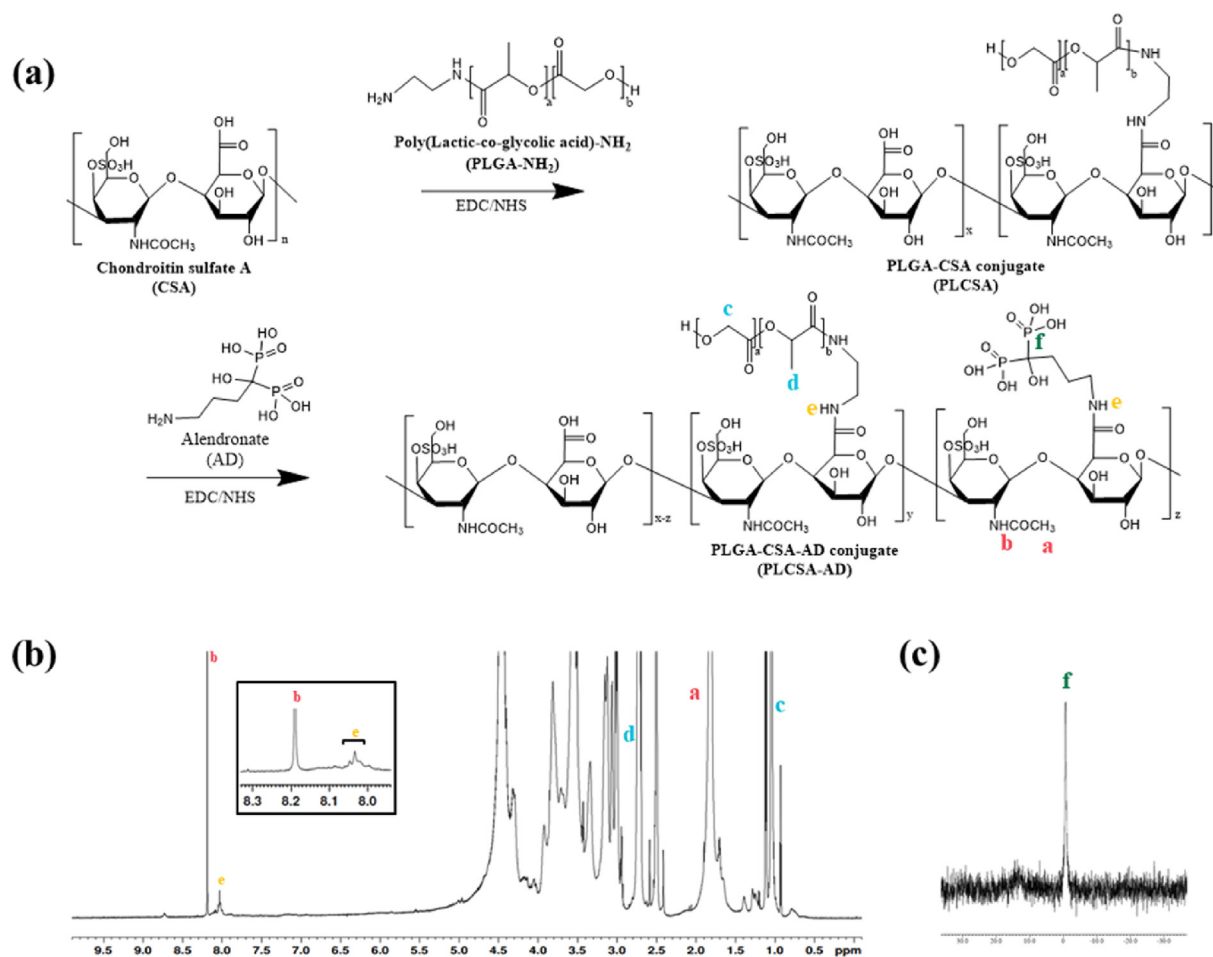
Fig. 2. Synthesis of PLCSA-AD. (a) Synthetic scheme of CSA-PLGA-AD conjugate (PLCSA-AD), and its verification by (b) ¹H NMR and (c) ³¹P NMR. The inset indicates ¹H NMR of amide bonds. Chemical shifts representing CSA (a, b) and PLGA (c, d) were assigned in the spectrum of PLCSA-AD. The polymer conjugate was dissolved in a mixture of DMSO-*d₆* and D₂O (1:1, v/v) for the NMR analyses.
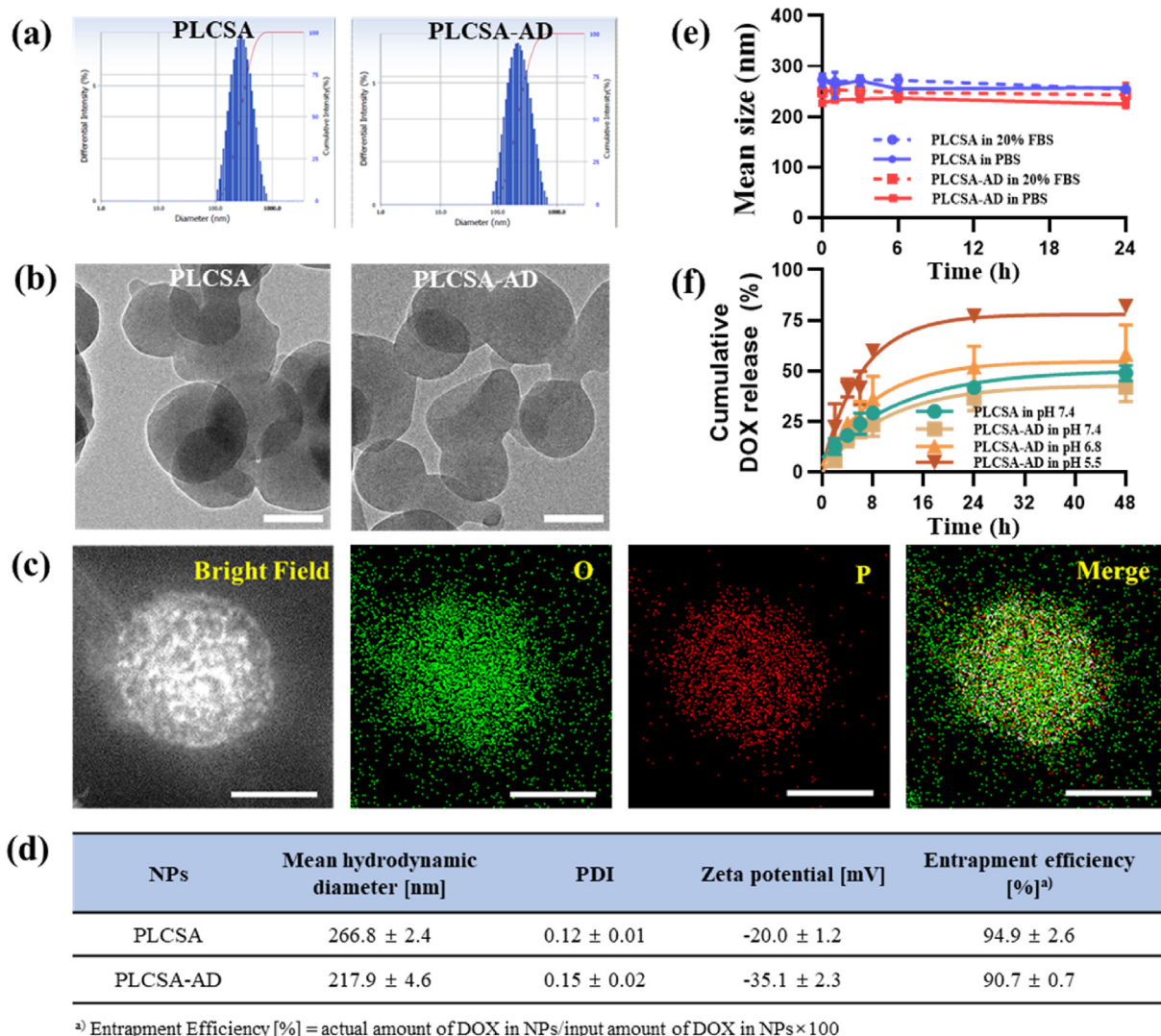
Fig. 3. Characterization of PLCSA-AD. (a) Histogram of size distribution and (b) field-emission transmission electron microscopy images. The length of the scale bar is 200 nm. (c) Atomic analysis of PLCSA-AD. White, green, and red colors indicate bright field, oxygen, and phosphorus, respectively. The length of the scale bar is 100 nm. (d) Summary of physicochemical properties. (e) Measurement of mean diameter in PBS or 20% FBS for 24 h. (f) *In vitro* DOX release profile under three different pH conditions. (For interpretation of the references to colour in this figure legend, the reader is referred to the Web version of this article.)

efficiently entrapped DOX inside their inner cavity, of which the entrapment efficiency was calculated as 94.9 ± 2.6% in PLCSA and 90.7 ± 0.7% in PLCSA-AD. Fig. 3e shows the colloidal stability of PLCSA and PLCSA-AD in biological fluids for up to 24 h. The mean diameters of both NTs were maintained in PBS. Similarly, the particle size showed no significant time-course changes in 20% FBS, without any sign of aggregation. These results imply that non-specific adsorption of serum components could be negligible after intravenous administration.

Fig. 3f shows *in vitro* DOX release profiles from PLCSA and PLCSA-AD at three different pH conditions, where pH 5.5, 6.8, and 7.4 corresponded to the pH of the endocytic compartment inside the tumor cell (*e.g.,* lysosome), TME, and normal physiological conditions (*e.g.,* plasma), respectively. The rate of DOX release increased significantly at pH 5.5, showing a 1.9-fold higher cumulative release after 48 h than at pH 7.4. The pH-dependent release pattern suggests that DOX exposure could be more selective in tumor tissues than in normal tissues, contributing to improved antitumor efficacy and safety [23,24]. Furthermore, the NTs showed a sustained DOX release over 48 h. The hydrophobic nature of the PLGA segment in NTs structure may contribute to this desirable release pattern for parenteral formulations [25]. To further investigate the release properties, each profile was fitted by four different

mathematical dissolution models (Table S1). Among these, the first-order model with F_{max} showed the highest correlation coefficient, indicating that the rate of DOX release was directly proportional to the concentration of the drug inside the NTs.

3.2. Cellular uptake and hydroxyapatite affinity tests in 2D bone tumor-mimicking cell culture model

To assess the tumor cell uptake and hydroxyapatite binding of NTs simultaneously, we developed a 2D bone tumor-mimicking cell culture model, wherein bone tumor cells were cultured in hydroxyapatite beads and collagen mixture-coated plates to mimic the mineralized bone TME [26]. In this investigation, HOS/MNNG was selected as a human osteosarcoma model cell line, given its high tumorigenicity and ability of colony-forming, invasion, and proliferation, which are characteristics of bone cancer [27]. In addition, hydroxyapatite beads served as non-toxic mineralized support to the tumor cells under the experimental conditions (Fig. S2).

Fig. 4a shows the fluorescence intensities of DAPI and DOX after incubation with NTs. The intensity of DOX increased significantly in NT-treated tumor cells, suggesting an improved cellular uptake efficiency
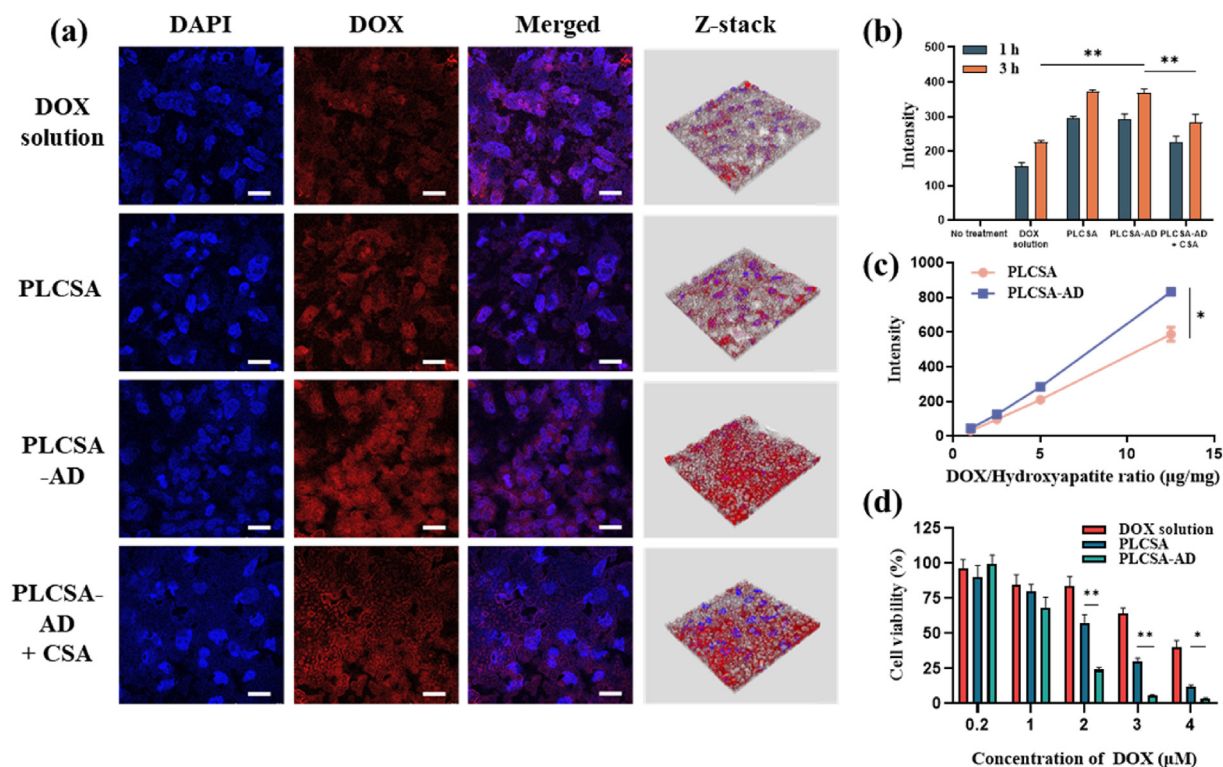
Fig. 4. *In vitro* cellular uptake and affinity for hydroxyapatites in 2D bone tumor-mimicking cell culture model. (a) CLSM images of 2D bone tumor-mimicking cell culture model after treatment. The length of the scale bar is 20 μm. (b, c) Flow cytometry analyses of (b) HOS/MNNG cells incubated for 1 or 3 h after treatment and (c) hydroxyapatite beads with various DOX/hydroxyapatite beads ratios. (d) MTS assay of HOS/MNNG cells after treatment. *$p < 0.0005$; **$p < 0.0001$.

compared with that of the DOX solution. This efficient cellular uptake could be explained by the interactions between CSA and its cognate receptors on the tumor cell surface, such as CD44, and subsequent receptor-mediated endocytosis [28,29]. The cellular uptake of PLCSA-AD significantly decreased when free CSA was added as a competitive inhibitor of surface receptors, which supports the involvement of the receptor-mediated endocytosis mechanism. Notably, the background intensity of the PLCSA-AD and PLCSA-AD + CSA groups was higher than that of the PLCSA group, suggesting a higher hydroxyapatite binding affinity for AD-decorated NTs than that of the unmodified ones. Moreover, the Z-stack images clearly showed a higher distribution of AD-conjugated NTs in the bone-matrix-mimicking layer compared with PLCSA.

To further confirm the hypothesis that the bisphosphonate group of AD might induce ionic interactions between hydroxyapatite and PLCSA-AD, the cellular uptake efficiency and hydroxyapatite-binding ability of PLCSA-AD were evaluated separately by flow cytometry. In tumor cells, the fluorescence intensity of DOX was significantly higher in the NT-treated groups than in the DOX solution-treated group, and the intensity of the PLCSA-AD group markedly decreased when free CSA was added (Fig. 4b). In hydroxyapatite beads after incubation with NTs, both PLCSA and PLCSA-AD showed a concentration-dependent adsorption pattern (Fig. 4c). As measured in Fig. 3d, the PLCSA itself had a sufficiently high negative surface charge (-20.0 ± 1.2 mV) to cause electrostatic attraction with hydroxyapatites, which explains the proportional increase in the fluorescence intensity with respect to the DOX/hydroxyapatite ratio. A higher negative surface charge by AD decoration (-35.1 ± 2.3 mV) provided PLCSA-AD with stronger adsorption ability than PLCSA, exhibiting a steeper line slope. These cytometric results are consistent with the CLSM images, suggesting that PLCSA-AD is localized effectively in the mineralized matrix of the bone TME, as well as in tumor cells.

In vitro cytotoxicity against HOS/MNNG cells was evaluated using the MTS assay (Fig. 4d). PLCSA and PLCSA-AD exhibited significantly lower

cell viability than the DOX solution, with IC$_{50}$ values of 3.043 ± 0.126 μM for the DOX solution, 2.202 ± 0.050 μM for PLCSA, and 1.269 ± 0.156 μM for PLCSA-AD. The enhanced antitumor activities of PLCSA and PLCSA-AD could be attributed to their higher cellular uptake efficiency compared with that of the DOX solution (Fig. 4b). Interestingly, PLCSA-AD exhibited significantly higher anticancer activity than that of PLCSA. It can be inferred that PLCSA-AD may have served as a chemosensitizer of DOX, considering that the cellular uptake efficiency of PLCSA and PLCSA-AD in the tumor-cell-alone model was almost the same (Fig. 4b) and that the blank polymers themselves (*i.e.,* PLCSA and PLCSA-AD without DOX) exhibited no cytotoxicity up to 1 mg/mL (Fig. S3).

3.3. Apoptotic process and mevalonate pathway inhibition

To further investigate the enhanced tumor-suppressive effects of PLCSA-AD observed in the cytotoxicity study (Fig. 4d), we analyzed NT-treated cells at the cellular and molecular levels. First, changes in membrane components and integrity were evaluated using annexin V-FITC/PI double staining (Fig. 5a). In the contour plots, the DOX solution and PLCSA induced early and late apoptosis of the tumor cells, leaving less than 15% live cells. Interestingly, PLCSA-AD further increased the early ($33.6 \pm 2.7\%$; $p < 0.001$), late ($60.5 \pm 0.7\%$; $p < 0.001$), and total ($94.1 \pm 2.0\%$; $p < 0.0001$) apoptosis compared with the PLCSA group ($22.2 \pm 0.6\%$ in early apoptosis; $57.2 \pm 0.7\%$ in late apoptosis; and $79.4 \pm 0.1\%$ in total apoptosis), which is consistent with the cell viability results.

Next, the expression and activation of apoptosis-related proteins were evaluated by western blot analyses, wherein four representative apoptotic markers were employed: p53 [30], FADD [31], caspase-3 [32], and caspase-9 [32]. In all treatment groups, the expression level of the proteins significantly increased compared with the untreated group (Fig. 5b and Fig. S4a). The increased expression of p53 and FADD indicates the induction of intrinsic and extrinsic apoptosis pathways. Notably, the PLCSA-AD-treated cells exhibited a higher amount of
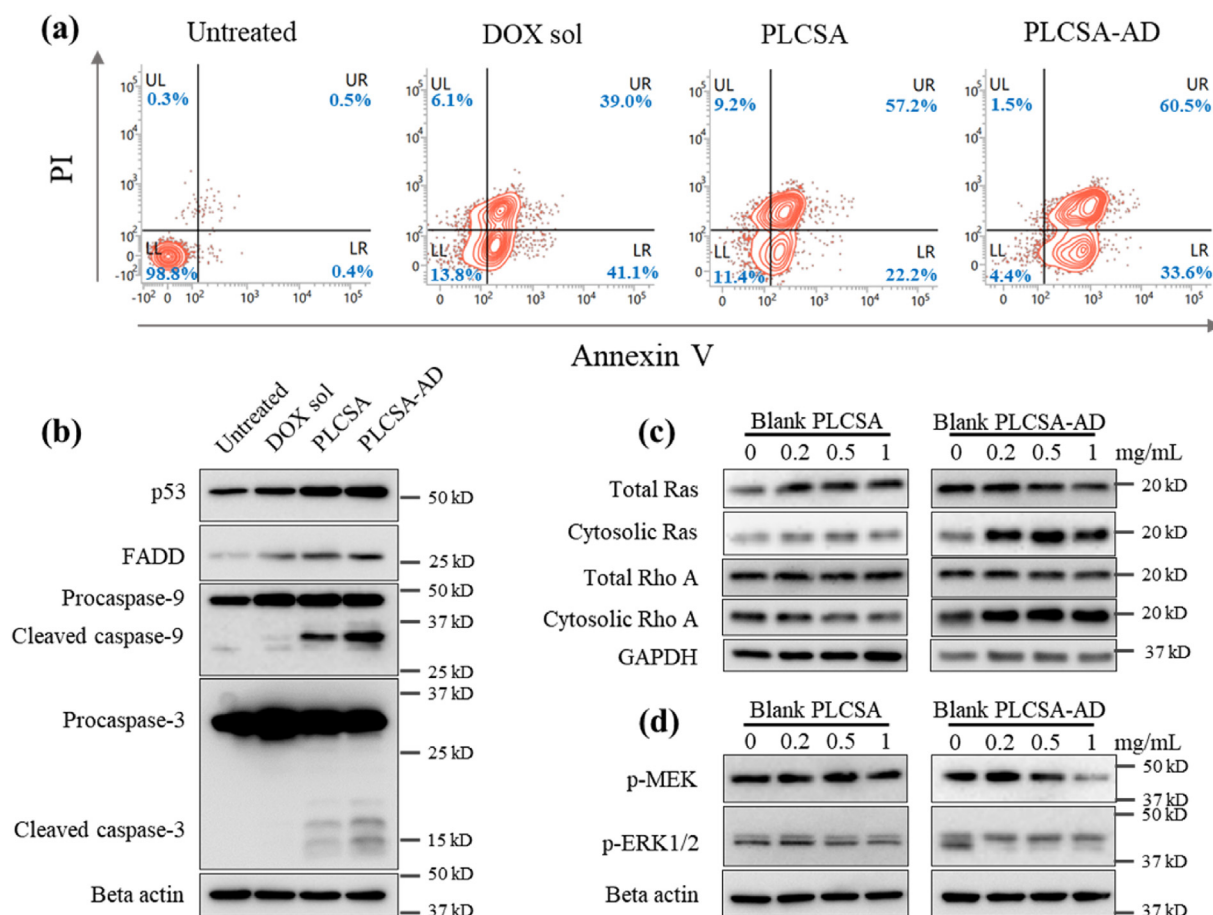
Fig. 5. Analyses of the apoptosis and mevalonate pathway inhibition in PLCSA-AD-treated HOS/MNNG cells. (a) Representative flow cytometry contour plots of HOS/MNNG cells stained with annexin V-FITC and PI. (b) Western blot analysis of representative apoptosis-related proteins after treatment with NTs. (c, d) Western blot analyses of (c) small GTPases and (d) the phosphorylated ERK1/2 and MEK after treatment with blank PLCSA or PLCSA-AD. The quantification of the Western blot images is available in the Supplementary Materials as Fig. S4.

cleaved caspase-3 (17 and 19 kDa) and cleaved caspase-9 (35 and 37 kDa) compared with PLCSA-treated cells, suggesting a greater activation of the procaspases for apoptosis. Based on protein expression and membrane integrity, it is clear that the decoration of AD contributed to apoptotic processes.

Mevalonate pathway inhibition was investigated by measuring the cytosolic fraction of two representative small GTPases (Ras and RhoA) that require prenylation for membrane translocation (Fig. 5c and Fig. S4b). Nitrogen-containing bisphosphonates, including AD, interfere with the prenylation of proteins by inhibiting farnesyl diphosphate synthase [6], thereby disturbing the translocation to membrane compartments [33,34]. When treated with blank PLCSA or PLCSA-AD at four different concentrations, the amounts of total Ras and RhoA displayed negligible changes, regardless of the concentration. However, only the PLCSA-AD group showed a significantly increased amount of cytosolic Ras and RhoA, which can be explained by decreased localization to membrane compartments. The prenylation inhibition of Ras and RhoA could lead to a decrease in functional activity, as well as localization [33]. To investigate the changes in the Ras-related biological process caused by its inhibition, MEK and ERK1/2, downstream components of the Ras/Raf/MEK/ERK signaling pathway, were analyzed (Fig. 5d and Fig. S4b) [35,36]. After treatment with blank PLCSA-AD for 72 h, the degree of phosphorylation of MEK (*i.e.*, *p*-MEK) and ERK1/2 (*i.e.*, *p*-ERK1/2) decreased significantly compared with that of blank PLCSA. Given that the pathway is crucial for cancer growth, development, and survival [35–37], the improved tumor-suppressive effects observed in

Figs. 4d and 5b can be explained by the synergistic effect of mevalonate pathway inhibition by AD.

3.4. In vivo tumor distribution in bone tumor-mimicking xenografted mouse model

The tumor distribution and retention of PLCSA-AD were evaluated using a bone tumor-mimicking xenografted mouse model, where a mixture of cell suspension and hydroxyapatite beads were co-inoculated subcutaneously into the mouse to simulate the mineralization of bone TME [26]. After tumor formation, the hydroxyapatite beads were localized in the extracellular matrix, providing a mineralized scaffold for the bone tumor cells (Fig. S5).

Fig. 6a and b shows the time-course whole-body scan images and average radiant efficiency (RE) values of the tumor region, respectively, after intravenous injection of Cy5.5-labeled NTs. A marked difference was observed in the tumor distribution patterns between PLCSA and PLCSA-AD. In the PLCSA group, the RE values of the tumor region (dotted circle) continuously decreased over 24 h. However, the PLCSA-AD group showed an increase in RE up to 9 h, exhibiting a 2.64-fold higher RE at 24 h compared with that of PLCSA. These data suggest that PLCSA-AD can provide more prolonged bone tumor distribution profiles than PLCSA, which can be primarily attributed to the enhanced cellular uptake and bone TME interactions caused by AD modification. The *ex vivo* biodistribution in the tumors and major organs (liver, heart, spleen, lung, and kidneys) was investigated 24 h after injection (Fig. 6c and d). Both
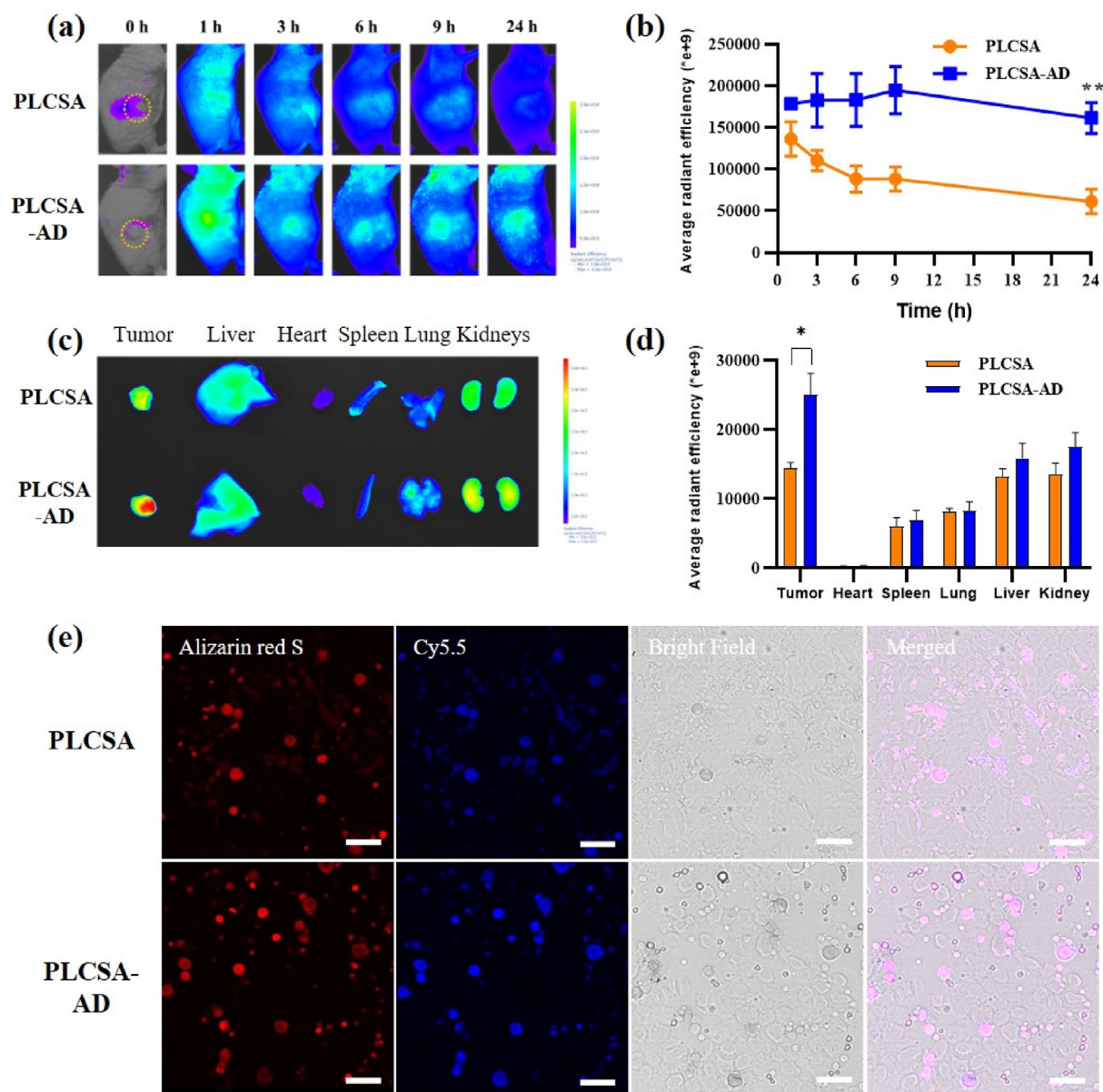
Fig. 6. *In vivo* NIRF images in bone tumor-mimicking mouse model. (a) Time-course whole-body scanning after intravenous injection of Cy5.5-labeled NTs. (b) Average radiant efficiency values in tumor region. (c) Representative image of the excised tumor and major organs at 24 h, and (d) their average radiant efficiency values. (e) CLSM images of sliced tumor at 24 h. The red and blue colors indicate alizarin red S and Cy5.5, respectively. The length of the scale bar is 20 μm *$p < 0.01$; **$p < 0.005$. (For interpretation of the references to colour in this figure legend, the reader is referred to the Web version of this article.)

PLCSA and PLCSA-AD showed the highest accumulation in tumors compared with other organs, suggesting excellent tumor-targeting ability. Notably, PLCSA-AD exhibited a 1.73-fold higher tumor disposition than PLCSA, which clearly indicates the enhanced bone tumor-homing ability conferred by AD decoration. Although PLCSA-AD showed slightly increased kidney accumulation compared to PLCSA ($p < 0.05$), this could be attributed to the bisphosphonate-specific transport mechanism in renal epithelial cells [38,39].

To investigate the hydroxyapatite-binding ability of the AD-decorated NTs *in vivo*, excised tumors were sliced and observed by CLSM (Fig. 6e). The slices of tumors were stained with alizarin red S to visualize the localization of hydroxyapatite beads [40]. The Cy5.5-labeled PLCSA-AD group showed greater Cy5.5 intensity (blue color) than Cy5.5-labeled PLCSA, which corresponds well with the *in vivo* and *ex vivo* imaging results. Interestingly, the Cy5.5 signal highly overlapped with the alizarin red S signal (red color) in the PLCSA-AD group. This observation strongly

suggests that the enhanced bone tumor accumulation could result from the increased affinity for hydroxyapatites by the AD groups.

3.5. In vivo antitumor activity

In vivo antitumor activities of PLCSA and PLCSA-AD were evaluated using a hydroxyapatite-containing xenograft mouse model. The mice were randomly divided into four groups: PBS (control), DOX solution, PLCSA, and PLCSA-AD, followed by three treatments, as scheduled (Fig. 7a). The PBS-treated mice exhibited rapid tumor growth, whereas the DOX solution- and NT-treated groups showed significantly retarded growth (Fig. 7b). As expected, the PLCSA-AD group showed more significant tumor suppression than the PLCSA group ($p < 0.01$). Based on *in vitro* cell studies and *in vivo* imaging, it is plausible that the enhanced tumor accumulation and apoptotic processes led to effective tumor suppression. The visual image and weight of excised tumors on day 12
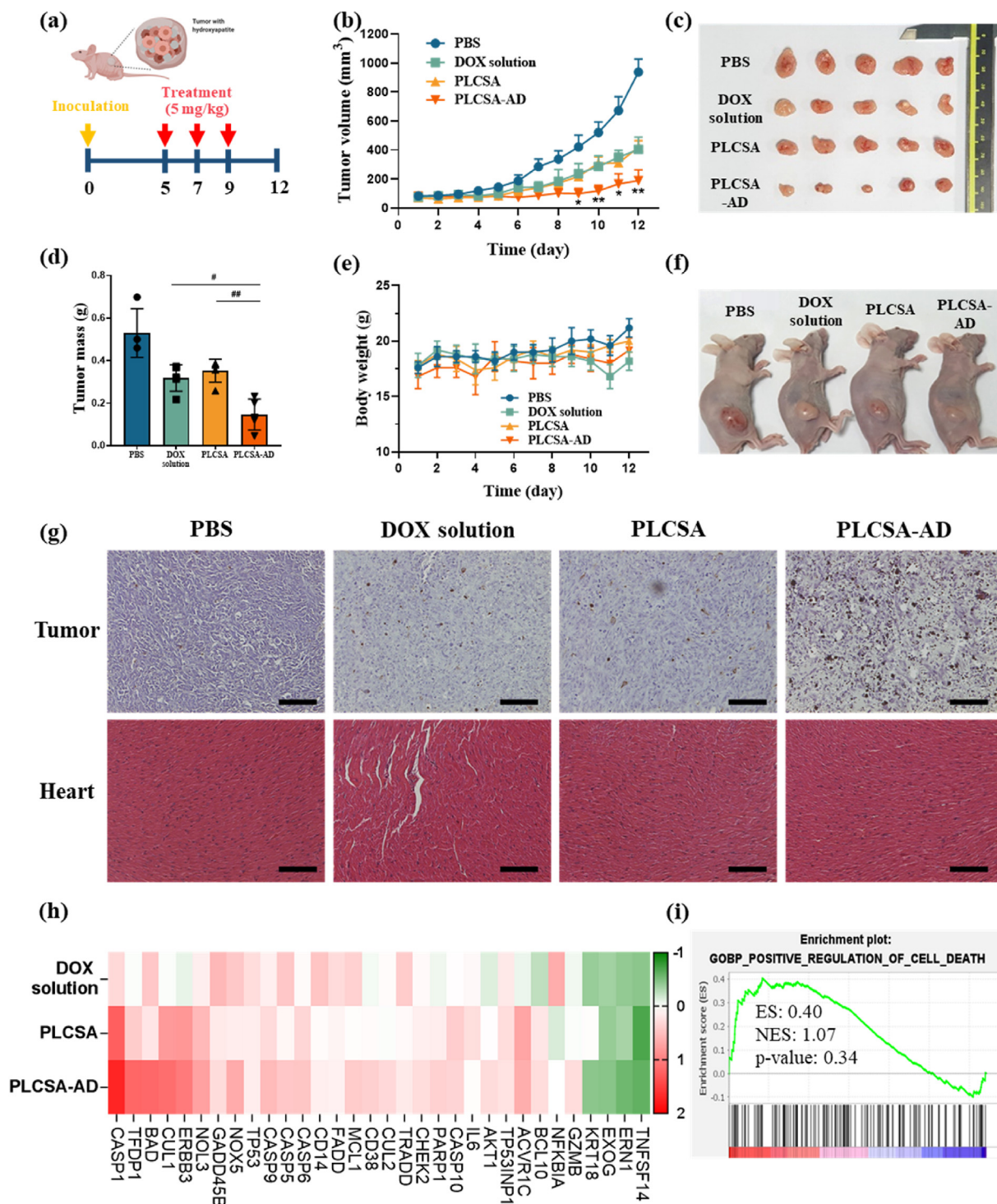
Fig. 7. *In vivo* antitumor efficacy tests. (a) Scheme for the bone tumor-mimicking mouse model and treatment schedule. (b) Tumor growth profile for 12 days after inoculation ($n = 5$). (c) Digital image of the dissected tumors on day 12, and (d) mass of the tumors. (e) Body weight change of the mice during the evaluation. (f) The appearance of a representative mouse from each group on day 12. (g) Histological analyses of tumor and heart, which were stained with TUNEL and H&E, respectively. (h) Heatmap of cell death-related protein expression in tumors after treatment, the level of which was compared with the tumor of PBS-treated mouse. The scale bar indicates fold-change. (i) Enrichment plot of the positive regulation of cell death in the PLCSA-AD group, analyzed based on the fold-change of the proteins in tumors. $^*p < 0.05$, $^{**}p < 0.01$, compared to other groups; $^{\#}p < 0.05$; $^{\#\#}p < 0.01$.

support the highest tumor-suppressive effect for PLCSA-AD compared with the other groups (Fig. 7c and d). Throughout the evaluation period, the body weight and appearance of NT-treated mice were not significantly different from those of PBS-treated mice (Fig. 7e and f), which may indicate no severe systemic toxicities.

Histological analysis demonstrated an enhanced apoptotic process in NT-treated tumors without severe cardiotoxicity (Fig. 7g). The excised tumor and heart were sliced and stained with TUNEL and H&E, respectively. The PBS group exhibited a high density of tumor cells (purple color) and a low number of brown spots (apoptotic cells), whereas the

DOX solution and PLCSA groups showed lower cell density and many brown spots, indicating DOX-induced apoptosis in tumors. Notably, the number of brown spots markedly increased in the PLCSA-AD group, suggesting augmentation of the apoptotic process. DOX-induced cardiotoxicity was assessed by histological examination of the heart. DOX solution-treated hearts clearly showed white striations and loss of myofibrils, implying cardiac damage over the treatment schedule [41]. Interestingly, the NT-treated mice did not show any significant cardiac damage, which might be attributed to the negligible cardiac distribution of NTs (Fig. 6d). The apoptotic process in the tumor was further investigated by screening for apoptosis-related protein expression patterns. Fig. 7h shows the representative protein expression as a relative fold-change with respect to the PBS-treated group. PLCSA-AD induces expression and activation of apoptosis-related proteins. GSEA results showed that PLCSA-AD treatment was positively correlated with the "positive regulation of cell death," suggesting apoptotic processes in the tumors (Fig. 7i). Additional immunohistochemical analyses were performed to verify the inhibition of the mevalonate pathway in tumors treated with PLCSA-AD (Fig. S6). As previously shown in Fig. 5c and d, the AD-decorated PLCSA hindered the RAS/RAF/MEK/ERK (MAPK) signaling pathway, which could explain the decreased expression of cyclin D1 [42,43] and increased expression of AMPK α1 [44,45] in the tumor tissues.

For further evaluation of biocompatibility, histological assays on the major organs were performed, where the NT-treated mice showed no apparent tissue damage in the liver, spleen, lungs, and kidneys (Fig. S7). The blood biochemistry and complete blood count of NT-treated mice also exhibited no significant differences compared with those of the control group (Fig. S8 and Table S2), excluding the risk of myelosuppression caused by DOX [46]. Therefore, it is highly probable that the developed NTs have excellent biocompatibility.

4. Conclusion

We developed bone tumor-homing polymeric nanotherapeutics (PLCSA-AD) for effective tumor suppression *via* prolonged tumor retention and inhibition of the mevalonate pathway. The NTs were composed of a novel graft copolymer of CSA and PLGA, and their surface was decorated with AD moieties that form strong ionic interactions with hydroxyapatite in the bone TME, improving their bone tumor accumulation. The increased affinity for hydroxyapatites and enhanced tumor accumulation were verified using *in vitro* and *in vivo* bone tumor-mimicking models. After uptake by tumor cells, PLCSA-AD inhibited the mevalonate pathway, providing a synergistic tumor-suppressive effect with DOX, which was confirmed by assessing the degree of localization of small GTPases and downstream metabolites. As a result, the developed NTs exhibited significantly higher therapeutic efficacy in bone tumor-bearing mice with excellent biocompatibility, suggesting that PLCSA-AD could be a promising drug delivery platform for bone tumor therapy.

Credit author statement

Nae-Won Kang: Conceptualization, Data curation, Formal analysis, Investigation, Methodology, Software, Validation, Visualization, Writing – original draft. **Voradanu Visetvichaporn**: Data curation, Formal analysis, Validation, Visualization. **Duy-Thuc Nguyen**: Formal analysis, Investigation, Methodology, Visualization. **Eun Kyung Shin**: Formal analysis, Investigation, Validation. **Da-Han Kim**: Investigation, Validation, Visualization. **Min-Jae Kim**: Formal analysis, Software, Visualization. **So-Yeol Yoo**: Formal analysis, Software, Validation, Visualization. **Jae-Young Lee**: Conceptualization, Data curation, Funding acquisition, Investigation, Methodology, Project administration, Validation, Visualization, Writing – original draft. **Dae-Duk Kim**: Conceptualization, Funding acquisition, Project administration, Resources, Supervision, Visualization, Writing – review & editing.

Declaration of competing interest

The authors declare that they have no known competing financial interests or personal relationships that could have appeared to influence the work reported in this paper.

Data availability

Data will be made available on request.

Appendix A. Supplementary data

Supplementary data to this article can be found online at https://doi.org/10.1016/j.mtbio.2023.100591.

References

[1] F. He, N.L. Springer, M.A. Whitman, S.P. Pathi, Y. Lee, S. Mohanan, S. Marcott, A.E. Chiou, B.S. Blank, N. Iyengar, P.G. Morris, M. Jochelson, C.A. Huids, P. Shah, J.A.M.R. Kunitake, L.A. Estroff, J. Lammerding, C. Fischbach, Hydroxyapatite mineral enhances malignant potential in a tissue-engineered model of ductal carcinoma in situ (DCIS), Biomaterials 224 (2019), 119489, https://doi.org/10.1016/j.biomaterials.2019.119489.

[2] J. Ritter, S.S. Bielack, Osteosarcoma, Ann. Oncol. 21 (2010) vii320–vii325, https://doi.org/10.1093/annonc/mdq276.

[3] F. He, A.E. Chiou, H.C. Loh, M. Lynch, B.R. Seo, Y.H. Song, M.J. Lee, R. Hoerth, E.L. Bortel, B.M. Willie, G.N. Duda, L.A. Estroff, A. Masic, W. Wagermaier, P. Fratzl, C. Fischbach, Multiscale characterization of the mineral phase at skeletal sites of breast cancer metastasis, Proc. Natl. Acad. Sci. U.S.A. 114 (2017) 10542–10547, https://doi.org/10.1073/pnas.1708161114.

[4] A. Gobel, V.M. Zinna, S.D. Endice, N. Jaschke, J.D. Kuhlmann, P. Wimberger, T.D. Rachner, Anti-tumor effects of mevalonate pathway inhibition in ovarian cancer, BMC Cancer 20 (2020) 703, https://doi.org/10.1186/s12885-020-07164-x.

[5] M. Thurnher, O. Nussbaumer, G. Gruenbacher, Novel aspects of mevalonate pathway inhibitors as antitumor agents, Clin. Cancer Res. 18 (2012) 3524–3531, https://doi.org/10.1158/1078-0432.CCR-12-0489.

[6] S.P. Luckman, D.E. Hughes, F.P. Coxon, R.G.G. Russell, M.J. Rogers, Nitrogen-containing bisphosphonates inhibit the mevalonate pathway and prevent post-translational prenylation of GTP-binding proteins, including ras, J. Bone Miner. Res. 13 (1998) 581–589, https://doi.org/10.1359/jbmr.1998.13.4.581.

[7] R. Zhang, X. Qin, F. Kong, P. Chen, G. Pan, Improving cellular uptake of therapeutic entities through interaction with components of cell membrane, Drug Deliv. 26 (2019) 328–342, https://doi.org/10.1080/10717544.2019.1582730.

[8] M.T. Drake, B.L. Clarke, S. Khosla, Bisphosphonates: mechanism of action and role in clinical practice, Mayo Clin. Proc. 83 (2008) 1032–1045, https://doi.org/10.4065/83.9.1032.

[9] A. Rubinstein, D. Nakar, A. Sintov, Chondroitin sulfate: a potential biodegradable carrier for colon-specific drug delivery, Int. J. Pharm. 84 (1992) 141–150.

[10] Y.-H. Chu, W.-C. Liao, Y.-J. Ho, C.-H. Huang, T.-J. Tseng, C.-H. Liu, Targeting chondroitin sulfate reduces invasiveness of glioma cells by suppressing CD44 and integrin β1 expression, Cells 10 (2021) 3594, https://doi.org/10.3390/cells10123594.

[11] L. Mayr, C. Pirker, D. Lotsch, S.V. Schoonhoven, R. Windhager, B. Englinger, W. Berger, B. Kubista, CD44 drives aggressiveness and chemoresistance of a metastatic human osteosarcoma xenograft model, Oncotarget 8 (2017) 114095–114108, https://doi.org/10.18632/oncotarget.23125.

[12] A. Gvozdenovic, M. Je Arlt, C. Campanile, P. Brennecke, K. Husmann, Y. Li, W. Born, R. Muff, B. Fuchs, CD44 enhances tumor formation and lung metastasis in experimental osteosarcoma and is an additional predictor for poor patient outcome, J. Bone Miner. Res. 28 (2013) 838–847, https://doi.org/10.1002/jbmr.1817.

[13] J.-Y. Lee, U. Termsarasab, M.Y. Lee, D.-H. Kim, S.Y. Lee, J.S. Kim, H.-J. Cho, D.-D. Kim, Chemosensitizing indomethacin-conjugated chitosan oligosaccharide nanoparticles for tumor-targeted drug delivery, Acta Biomater. 57 (2017) 262–273, https://doi.org/10.1016/j.actbio.2017.05.012.

[14] J.-Y. Lee, S.-J. Chung, H.-J. Cho, D.-D. Kim, Phenylboronic acid-decorated chondroitin sulfate A-based theranostic nanoparticles for enhanced tumor targeting and penetration, Adv. Funct. Mater. 25 (2015) 3705–3717, https://doi.org/10.1002/adfm.201500680.

[15] J.-Y. Lee, H.S. Lee, N.-W. Kang, S.Y. Lee, D.H. Kim, S. Kim, I.-S. Yoon, H.-J. Cho, D.-D. Kim, Blood component ridable and CD44 receptor targetable nanoparticles based on a maleimide-functionalized chondroitin sulfate derivative, Carbohydr. Polym. 230 (2020), 115568, https://doi.org/10.1016/j.carbpol.2019.115568.

[16] A.A. Reszka, G.A. Rodan, Nitrogen-containing bisphosphonate mechanism of action, Mini Rev. Med. Chem. 4 (2004) 711–719, https://doi.org/10.2174/1389557043403648.

[17] M.K. Tsoumpra, J.R. Muniz, B.L. Barnett, A.A. Kwaasi, E.S. Pilka, K.L. Kavanagh, A. Evdokimov, R.L. Walter, F.V. Delft, F.H. Ebetino, U. Oppermann, R.G.G. Russell, J.E. Dunford, The inhibition of human farnesyl pyrophosphate synthase by nitrogen-containing bisphosphonates. Elucidating the role of active site threonine 201 and tyrosine 204 residues using enzyme mutants, Bone 81 (2015) 478–486, https://doi.org/10.1016/j.bone.2015.08.020.

[18] J. Park, V.R. Pandya, S.J. Ezekiel, A.M. Berghuis, Phosphonate and bisphosphonate inhibitors of farnesyl pyrophosphate synthases: a structure-guided perspective, Front. Chem. 8 (2021), 612728, https://doi.org/10.3389/fchem.2020.612728.

[19] S.-Y. Yoo, Y.-H. Mun, N.-W. Kang, J.M. Koo, D.H. Lee, J.H. Yoo, S.M. Lee, S. Koh, J.C. Park, T. Kim, E.K. Shin, H.S. Lee, J. Sim, K.W. Kang, S.K. Kim, C.-W. Cho, M.G. Kim, D.-D. Kim, J.-Y. Lee, Enhancement of the therapeutic efficacy of the MAP regimen using thiamine pyrophosphate-decorated albumin nanoclusters in osteosarcoma treatment, Bioeng. Transl. Med. (2022), e10472, https://doi.org/10.1002/btm2.10472.

[20] H.K. Makadia, S.J. Siegel, Poly lactic-co-glycolic acid (PLGA) as biodegradable controlled drug delivery carrier, Polymers 3 (2011) 1377–1397, https://doi.org/10.3390/polym3031377.

[21] S.K. Hobbs, W.L. Monsky, F. Yuan, W.G. Roberts, L. Griffith, V.P. Torchilin, R.K. Jain, Regulation of transport pathways in tumor vessels: role of tumor type and microenvironment, Proc. Natl. Acad. Sci. USA 95 (1998) 4607–4612, https://doi.org/10.1073/pnas.95.8.4607.

[22] S. Bhattacharjee, DLS and zeta potential – what they are and what they are not? J. Contr. Release 235 (2016) 337–351, https://doi.org/10.1016/j.jconrel.2016.06.017.

[23] L.J.C. Albuquerque, V. Sincari, A. Jager, J. Kucha, J. Humajova, J. Pankrac, P. Paral, T. Heizer, O. Janouskova, I. Davidovich, Y. Talmon, P. Pouckova, P. Stepanek, L. Sefc, M. Hruby, F.C. Giacomelli, E. Jager, pH-responsive polymersome-mediated delivery of doxorubicin into tumor sites enhances the therapeutic efficacy and reduces cardiotoxic effects, J. Contr. Release 332 (2021) 529–538, https://doi.org/10.1016/j.jconrel.2021.03.013.

[24] R. Gannimani, P. Walvekar, V.R. Naidu, T.M. Aminabhavi, T. Govender, Acetal containing polymers as pH-responsive nano-drug delivery systems, J. Contr. Release 328 (2020) 736–761, https://doi.org/10.1016/j.jconrel.2020.09.044.

[25] J.K. Patra, G. Das, L.F. Fraceto, E.V.R.C. Campos, M.D.P. Rodriguez-Torres, L.S. Acosta-Torres, L.A. Diaz-Torres, R. Grillo, M.K. Swamy, S. Sharma, S. Habtemariam, H.-S. Shin, Nano based drug delivery systems: recent developments and future prospects, J. Nanobiotechnol. 16 (2018) 7, https://doi.org/10.1186/s12951-018-0392-8.

[26] N.-W. Kang, J.-Y. Lee, D.-D. Kim, Hydroxyapatite-binding albumin nanoclusters for enhancing bone tumor chemotherapy, J. Contr. Release 342 (2022) 111–121, https://doi.org/10.1016/j.jconrel.2021.12.039.

[27] S.U. Lauvrak, E. Munthe, S.H. Kresse, E.W. Stratford, H.M. Namlos, L.A. Meza-Zepeda, O. Myklebost, Functional characterization of osteosarcoma cell lines and identification of mRNAs and miRNAs associated with aggressive cancer phenotypes, Br. J. Cancer 109 (2013) 2228–2236, https://doi.org/10.1038/bjc.2013.549.

[28] T. Fujimoto, H. Kawashima, T. Tanaka, M. Hirose, N. Toyama-Sorimachi, Y. Matsuzawa, M. Miyasaka, CD44 binds a chondroitin sulfate proteoglycan, aggrecan, Int. Immunol. 13 (2001) 359–366, https://doi.org/10.1093/intimm/13.3.359.

[29] H. Yan, O.P. Oommen, D. Yu, J. Hilborn, H. Qian, O.P. Varghese, Chondroitin sulfate-coated DNA-nanoplexes enhance transfection efficiency by controlling plasmid release from endosomes: a new insight into modulating nonviral gene transfection, Adv. Funct. Mater. 25 (2015) 3907–3915, https://doi.org/10.1002/adfm.201500695.

[30] J.S. Fridman, S.W. Lowe, Control of apoptosis by p53, Oncogene 22 (2003) 9030–9040, https://doi.org/10.1038/sj.onc.1207116.

[31] A.M. Chinnaiyan, K. O'Rourke, M. Tewari, V.M. Dixit, FADD, a novel death domain-containing protein, interacts with the death domain of fas and initiates apoptosis, Cell 81 (1995) 505–512, https://doi.org/10.1016/0092-8674(95)90071-3.

[32] M. Brentnall, L. Rodriguez-Menocal, R.L.D. Guevara, E. Cepero, L.H. Boise, Caspase-9, caspase-3 and caspase-7 have distinct roles during intrinsic apoptosis, BMC Cell Biol. 14 (2013) 1–9, https://doi.org/10.1186/1471-2121-14-32.

[33] C.C. Palsuledesai, M.D. Distefano, Protein prenylation: enzymes, therapeutics, and biotechnology applications, ACS Chem. Biol. 10 (2015) 51–62, https://doi.org/10.1021/cb500791f.

[34] M. Wang, P.J. Casey, Protein prenylation: unique fats make their mark on biology, Nat. Rev. Mol. Cell Biol. 17 (2016) 110–122, https://doi.org/10.1038/nrm.2015.11.

[35] P.J. Roberts, Cj Der, Targeting the Raf-MEK-ERK mitogen-activated protein kinase cascade for the treatment of cancer, Oncogene 26 (2007) 3291–3310, https://doi.org/10.1038/sj.onc.1210422.

[36] S. Yang, G. Liu, Targeting the Ras/Raf/MEK/ERK pathway in hepatocellular carcinoma (review), Oncol. Lett. 13 (2017) 1041–1047, https://doi.org/10.3892/ol.2017.5557.

[37] Y.-J. Guo, W.-W. Pan, S.-B. Biu, Z.-F. Shen, Y. Xu, L.-L. Hu, ERK/MAPK signaling pathway and tumorigenesis (review), Exp. Ther. Med. 19 (2020) 1997–2007, https://doi.org/10.3892/etm.2020.8454.

[38] I. Kino, Y. Kato, J.H. Lin, Y. Sugiyama, Renal handling of biphosphonate alendronate in rats, Biopharm. Drug Dispos. 20 (1999) 193–198, https://doi.org/10.1002/(sici)1099-1081x(199905).

[39] U. Troehler, J.P. Bonjour, H. Fleisch, Renal transport of bisphosphonates: accumulation by renal cortical slices enhanced by calcium phosphate ions, J. Lab. Clin. Med. 106 (1985) 23–29.

[40] B.P.J. Fournier, F.C. Ferre, L. Couty, J.-J. Lataillade, M. Gourven, A. Naveau, B. Coulomb, A. Lafont, B. Gogly, Multipotent progenitor cells in gingival connective tissue, Tissue Eng. 16 (2010) 2891–2899, https://doi.org/10.1089/ten.tea.2009.0796.

[41] S. Zhang, X. Liu, T. Bawa-Khalfe, L.-S. Lu, Y.L. Lyu, L.F. Liu, E.T.H. Yeh, Identification of the molecular basis of doxorubicin-induced cardiotoxicity, Nat. Med. 18 (2012) 1639–1642, https://doi.org/10.1038/nm.2919.

[42] P.K. Modi, N. Komaravelli, N. Singh, P. Sharma, Interplay between MEK-ERK signaling, cyclin D1, and cyclin-dependent kinase 5 regulates cell cycle reentry and apoptosis of neurons, Mol. Biol. Cell 23 (2012) 3722–3730, https://doi.org/10.1091/mbc.e12-02-0125.

[43] I. Gkouveris, N. Nikitakis, M. Karanikou, G. Rassidakis, A. Sklavounou, Erk1/2 activation and modulation of STAT3 signaling in oral cancer, Oncol. Rep. 32 (2014) 2175–2182, https://doi.org/10.3892/or.2014.3440.

[44] S.-L. Hwang, Y.-T. Jeong, X. Li, Y.D. Kim, Y. Lu, Y.-C. Chang, I.-K. Lee, H.W. Chang, Inhibitory cross-talk between the AMPK and ERK pathways mediates endoplasmic reticulum stress-induced insulin resistance in skeletal muscle, Br. J. Pharmacol. 169 (2013) 69–81, https://doi.org/10.1111/bph.12124.

[45] I. Kawashima, T. Mitsumori, Y. Nozaki, T. Yamamoto, Y. Shobu-Sueki, K. Nakajima, K. Kirito, Negative regulation of the LKB1/AMPK pathway by ERK in human acute myeloid leukemia cells, Exp. Hematol. 43 (2015) 524–533, https://doi.org/10.1016/j.exphem.2015.03.005.

[46] M.B. Bally, R. Nayar, D. Masin, P.R. Cullis, L.D. Mayer, Studies on the myelosuppressive activity of doxorubicin entrapped in liposomes, Cancer Chemother. Pharmacol. 27 (1990) 13–19, https://doi.org/10.1007/BF00689270.